



**HAL**  
open science

## Estimation of Cavitation Pit Distributions by Acoustic Emission

Markku Ylönen, Pentti Saarenrinne, Juha Miettinen, Jean-Pierre Franc, Marc C. Fivel, Jarmo Laakso

► **To cite this version:**

Markku Ylönen, Pentti Saarenrinne, Juha Miettinen, Jean-Pierre Franc, Marc C. Fivel, et al.. Estimation of Cavitation Pit Distributions by Acoustic Emission. *Journal of Hydraulic Engineering*, 2020, 146 (2), pp.04019064. 10.1061/(ASCE)HY.1943-7900.0001686 . hal-02408704

**HAL Id: hal-02408704**

**<https://hal.science/hal-02408704>**

Submitted on 3 Apr 2020

**HAL** is a multi-disciplinary open access archive for the deposit and dissemination of scientific research documents, whether they are published or not. The documents may come from teaching and research institutions in France or abroad, or from public or private research centers.

L'archive ouverte pluridisciplinaire **HAL**, est destinée au dépôt et à la diffusion de documents scientifiques de niveau recherche, publiés ou non, émanant des établissements d'enseignement et de recherche français ou étrangers, des laboratoires publics ou privés.

# Estimation of Cavitation Pit Distributions by Acoustic Emission

Markku Ylönen<sup>1</sup>; Pentti Saarenrinne<sup>2</sup>; Juha Miettinen<sup>3</sup>;  
Jean-Pierre Franc<sup>4</sup>; Marc Fivel<sup>5</sup>; and Jarmo Laakso<sup>6</sup>

**Abstract:** Cavitation erosion in hydraulic machinery, such as in turbines and pumps, often leads to significant reduction of the service life of the affected components, with serious consequences for their maintenance costs and operation efficiency. In this study, the potential contribution of acoustic emission (AE) measurements to the assessment of cavitation damage is evaluated from experiments in a cavitation tunnel. Stainless steel samples were exposed to cavitation and damage was characterized from pitting tests carried out on mirror-polished samples. The pits were measured using an optical profilometer and cavitation damage was characterized by pit diameter distribution. In parallel, AE time signal was measured directly from behind the samples. A dedicated signal-processing technique was developed in order to identify each burst in the AE signal and determine its amplitude. The AE amplitude distribution compares well with PVDF and pressure sensor measurements from literature. It is concluded that AE signal analysis can be used to monitor the formation of pits without visual examination of the damaged surface. This provides a basis for possible future applications of nonintrusive cavitation erosion monitoring in hydraulic machines, provided the findings remain true in a more complex environment.

## Introduction

Cavitation is a major source of malfunctions in pumps, turbines, and other modern hydraulic applications (Arndt et al. 1989). Cavitation erosion is negligible, for example, in hydraulic turbines operated at their designed optimum conditions. However, the modern tendency is to operate turbines as regulating power sources in the electric grid, because they are flexible and respond quickly to changing power output requirements. This flexibility does not come without a cost. When a turbine is operated outside its best operation point, erosive cavitation may occur. Additionally, quick ramping cannot always be avoided and it can lead to extremely high

loads and cavitation effects (Chirag et al. 2018). Some erosion might be tolerated, and some may be avoided, for example, by aerating the areas prone to cavitation (Penghua and James 2018; Gangfu and Hubert 2018), but in-situ knowledge of the actual erosion rate is limited. In these situations, monitoring cavitation damage in real time would be beneficial. The usual way to assess cavitation damage is to visually inspect the turbine during shutdowns in turbine revisions, and repair the turbines if there is too much damage. If reliable information was available during operation, unnecessary shutdowns and costly inspections could be avoided.

To understand the changes in the cavitation behavior of a machine, it would be beneficial to know the cavitation aggressiveness at different operating points. The first step towards such knowledge is to identify how cavitation impacts are distributed in a test rig that isolates cavitation from other phenomena. In this study, cavitation was created on a stainless steel sample in a high-speed cavitation tunnel (PREVERO 2018) and the pits caused by collapsing cavitation bubbles were detected and characterized through acoustic emission (AE) measurements and signal processing.

AE is defined as elastic waves traveling in a solid at a frequency above human hearing threshold (Holroyd 2000; Grosse 2008), typically in the range of 100 kHz to 1 MHz. These waves are detectable by acoustic emission sensors that are sensitive to surface deformations (Ohtsu 2008). The advantage of the AE monitoring method is that AE sensors can be placed outside the cavitation tunnel and there is no need to insert any sensors in the liquid flow. Additional benefits include low cost and fast installation. Only a good transfer path through solid materials is required. The main challenges lie in the interpretation of the data.

AE has been successfully used in monitoring cavitation, with different approaches than the one presented here. Neill et al. (1997) and Poddar and Tandon (2016) were able to detect cavitation incipience, their methods being based on the AE signals root mean squared (RMS) values that increase in amplitude and increasingly fluctuate when cavitation occurs. Analyzing parameters such as RMS and AE event energy and their fluctuation is a common approach, with typically good results (Boorsma and Fitzsimmons 2009;

---

<sup>1</sup>Doctoral Student, Faculty of Engineering and Natural Sciences, Tampere Univ., Korkeakoulunkatu 6, Tampere 33720, Finland (corresponding author). ORCID: <https://orcid.org/0000-0002-0092-2537>. Email: [markku.ylonen@tuni.fi](mailto:markku.ylonen@tuni.fi)

<sup>2</sup>Emeritus Professor, Faculty of Engineering and Natural Sciences, Tampere Univ., Korkeakoulunkatu 6, Tampere 33720, Finland. ORCID: <https://orcid.org/0000-0003-0279-2884>. Email: [pentti.saarenrinne@tuni.fi](mailto:pentti.saarenrinne@tuni.fi)

<sup>3</sup>Docent, Faculty of Engineering and Natural Sciences, Tampere Univ., Korkeakoulunkatu 6, Tampere 33720, Finland. ORCID: <https://orcid.org/0000-0002-4485-7140>. Email: [juha.miettinen@tuni.fi](mailto:juha.miettinen@tuni.fi)

<sup>4</sup>Emeritus Professor, Grenoble Institut d'ingénierie Université Grenoble Alpes, Laboratoire des Écoulements Géophysiques et Industriels, Univ. Grenoble Alpes, 1209-1211 Rue de la Piscine, Grenoble 38000, France. Email: [jean-pierre.franc@legi.cnrs.fr](mailto:jean-pierre.franc@legi.cnrs.fr)

<sup>5</sup>CNRS Research Professor, Grenoble Institut d'ingénierie Université Grenoble Alpes, Science et Ingénierie des Matériaux et Procédés, Univ. Grenoble Alpes, 101 Rue de la Physique BP46, 38000 Grenoble, France. Email: [marc.fivel@simap.grenoble-inp.fr](mailto:marc.fivel@simap.grenoble-inp.fr)

<sup>6</sup>Project Researcher, Faculty of Engineering and Natural Sciences, Tampere Univ., Korkeakoulunkatu 6, Tampere 33720, Finland. Email: [jarmo.laakso@tuni.fi](mailto:jarmo.laakso@tuni.fi)

Boorsma and Whitworth 2011; Schmidt et al. 2014, 2015; Look et al. 2018). However, these calculated parameters lack the detection of individual cavitation impacts, as they tend to be temporally so close to each other that the parameter averaging interprets them as one. The enveloping and peak counting method developed in this study reliably distinguishes individual events, thus providing additional useful information.

Other methods to distinguish individual events include conventional pressure sensors (Franc et al. 2011) and polyvinylidene fluoride (PVDF) sensors that are thin piezoelectric pressure sensors (Hujer et al. 2015; Momma and Lichtarowicz 1995; Wang and Chen 2007; Carrat et al. 2017; Arndt et al. 1997). Notably, the measurements by Hujer et al. (2015) and Franc et al. (2011), which were carried out in the same tunnel, provided exponential cumulative distributions similar to the results extracted from AE signals of this study. Their results were used for qualitative comparison. This proved that the obtained distributions are of the expected type and that AE captures the right events.

The pressures involved in a single cavitation bubble collapse may reach the order of several GPa, as modelled numerically by Hsiao et al. (2014). In the cavitation tunnel used for the current study, the impact loads may be up to 6 GPa in the most aggressive operation condition as estimated by Roy et al. (2015a, b), using an inverse finite element method. They also found that the pit diameters correlate with the bubble size, while the shape factor, which is the ratio between pit depth and pit diameter, correlates with the impact loads. This paper presents relations between distributions of AE peak voltage values and pit diameters. The assumption is that while the pit diameters correlate with bubble size, the bubble size is correlated to the total impact energy and thus the damage potential of the bubble collapse event. The main outcome of this work serves as a basis in moving towards cavitation detection by AE in hydraulic machinery.

## Experimental Program

The aim of this study is to determine a correlation between AE amplitude peak values and pit sizes during the cavitation incubation period. The underlying idea is that the collapse of a cavitation structure should induce both a peak in the acoustic emission signal and a pit on the material surface, provided its intensity is sufficiently high in comparison with the material yield strength. As a result, a strong correlation is expected between the AE peak rate and the pitting rate. To find this correlation, AE was measured from a sample experiencing pitting in a cavitation tunnel (PREVERO 2018). Two tests were conducted with different cavitation aggressiveness, one with a 2 MPa and the other with a 4 MPa tunnel upstream pressure. A higher upstream pressure generates a higher flow velocity and consequently a more aggressive cavitation. It should be noted that the cavitation number was kept constant for the two operating points so that the development of the cavitation structure remained similar and only its intensity was varied. For these two conditions (2 and 4 MPa upstream pressures), the duration of these tests was 6 and 2 min, respectively.

### Cavitation Tunnel and Sample Preparation

The experiments were conducted in the PREVERO cavitation tunnel in the LEGI laboratory, Grenoble, France (PREVERO 2018). The cavitation tunnel has a radially diverging test section and it is used for accelerated cavitation erosion testing. The downstream pressure of the tunnel may be varied from ambient pressure to up to 3 MPa absolute pressure, and the upstream pressure may be varied from ambient pressure to up to 4 MPa absolute pressure. The downstream pressure is controlled using a pressurized nitrogen

reservoir, and the upstream pressure is regulated by the rotation speed of the circulating pump. The typical temperature rise is in the order of 1°C per hour. Therefore, the temperature rises during the 2- and 6-min tests of this study were not measurable with the current setup and they were assumed to be insignificant.

The test section consists of a nozzle leading to a radially diverging section with a cross-section area smaller than that of the nozzle. The nozzle guides a high-speed water jet towards the stagnation point in the middle of a 100-mm diameter cylindrical material sample, which is flush-mounted to the flow channel. The flow turns 90° and diverges in all directions along the tested sample plane, as the channel transforms to a 2.5-mm thick radially diverging section. When the flow moves from the nozzle to the radial section, the cross-section area of the flow drops by 37.5%. With suitable operating parameters, the static pressure at the inlet of the radially diverging section falls below the critical pressure limit for cavitation inception, assumed to be close to the saturated vapor pressure. Further downstream, as the cross-section area increases, the static pressure increases and the cavitation structures collapse, thus damaging the sample placed in the test section.

Fig. 1(a) presents the cavitation tunnel's simplified schematics, with the downstream tank, pump, and pressure and temperature measurements. The pressures are measured at about 200 mm upstream and downstream from the test section and the pressure loss because of pipe flow is negligible compared to that in the test section. The test section marked in Fig. 1(a) is presented in detail in Fig. 1(b). The flow is diverted after it stagnates in the middle of the inflow nozzle and it is therefore parallel to the sample surface when cavitation occurs. Note that the eroded sample shown in Fig. 1(b) was selected for illustration purposes only, and it is not the same sample that was used in the present study. The one in the figure was eroded for a long duration, much longer than the incubation period length, and it is presented here to visualize the maximum erosion zone. The microscopic pits typical to the incubation period would not be visible in such a photograph. The AE sensor was attached to the sample with the aid of a waveguide, explained further in the text. The dimensions for the waveguide, the tunnel, or the test section are not in scale in Fig. 1.

When the cavitation tunnel is operated at the same cavitation number  $\sigma$ , the cavitation damage is always located at the same radial position of the cylindrical sample (Gavaises et al. 2015). The cavitation number in the tunnel is defined by Franc et al. (2012)

$$\sigma = \frac{P_d - P_v}{P_u - P_d} \quad (1)$$

where  $P_d$  = pressure downstream of the test section,  $P_u$  = pressure upstream of the test section, and  $P_v$  = the liquid's saturated vapor pressure. A typical value  $\sigma = 0.87$  is selected in order to locate the pitting zone at a radius of 22 mm [Fig. 1(b)]. To match the cavitation number, the downstream pressure is adjusted to  $P_d = 1.86$  MPa for the 4 MPa upstream pressure and to  $P_d = 0.93$  MPa for the 2 MPa upstream pressure.

The material samples in this study were made of a typical stainless steel used in Francis turbine runner blades. The material chemical composition, measured using optical spectrometry, is presented in Table 1.

The material had a tensile yield strength of 808 MPa (0.2% plastic strain) and an ultimate tensile strength of 870 MPa. The microstructure was analyzed by polishing and etching a sample and then observing it with an optical microscope. The microstructure consisted of almost 100% of martensitic phase, with a prior austenite grain size of 109  $\mu\text{m}$ . The material properties are presented only for the record and they were not thoroughly analyzed here, as they are out of the focus of this study.

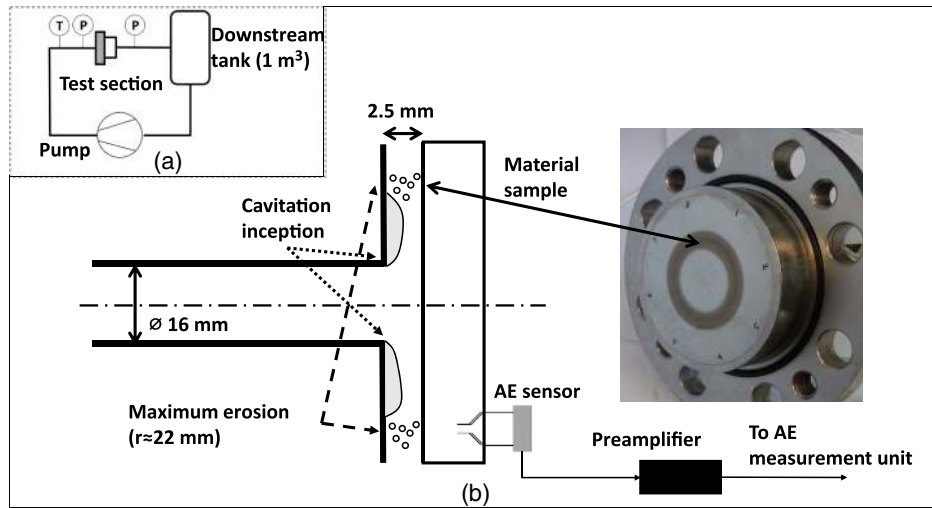


Fig. 1. (a) PREVERO cavitation schematics; and (b) tunnel test sections details and material sample.

Table 1. Material chemical composition

Element	Chemical composition (%)
Fe	81.7
C	0.02
Cr	12.6
Si	0.5
Mn	0.6
P	0.03
S	0.005
Ni	4.2
Mo	0.5

Two samples were prepared, one for each pitting test. The samples were 100-mm diameter and 20-mm thick cylindrical disks, with three screw threads machined in the face opposed to the exposed surface. One thread in the middle to fix the sample in the sample holder and two at diametrically opposed positions and a radial location of 22.5 mm to fix the acoustic emission waveguides into them [Fig. 1(b)]. The flow-side face was mirror-polished. The polishing was performed by grinding the sample with sandpapers of different grit sizes, followed by a polishing step with successive diamond pastes (3- and 1- $\mu\text{m}$  grain size) and finally with a colloidal silica suspension (0.03- $\mu\text{m}$  grain size).

### Pit Detection by Profilometry

To detect and characterize the pits resulting from cavitation, the sample surface was analyzed by an Alicona Infinitefocus G5 optical profilometer. The measurement technique was microscopy-like imaging based on depth measurement by focus variation. The imaging was done with the aid of a white light source. Light passed to the sample surface through illumination optics, a semitransparent mirror, and an objective lens. Because of the variation in the topography and reflectivity of the sample surface, the light reflected to different directions and partly back to the objective. That light proceeded through imaging mirrors and optics to the charge-coupled device (CCD camera) sensor for focally detecting individual points. The vertical focal position was varied to create sharp images. The altitude coordinate of each point was calculated, from the focal positions in the final sharp image. Fig. 2 presents a typical individual pit imaged by the optical profilometer, with a slightly better

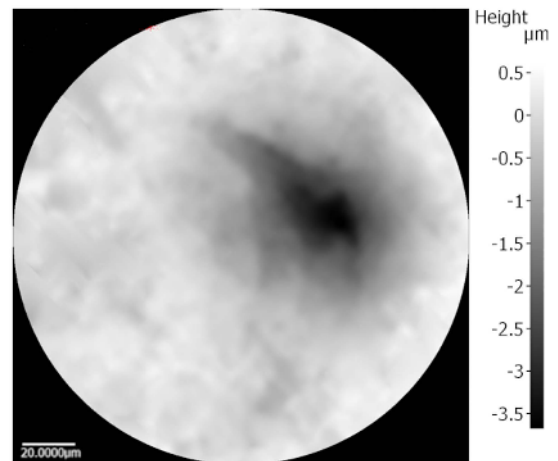


Fig. 2. Individual pit imaged by the profilometer.

resolution than used for the measurements performed on the entire eroded sample surface.

The sample surface was mirror-like, excluding the pits that were less reflective than the virgin surface. The pits, such as in Fig. 2, were captured rigorously, but the high reflectivity of the nondamaged surface provided some challenges. In this study, a polarizer was used to generate polarized light illumination and the reflected light was then filtered before it reached the CCD sensor.

The surface topography of the samples were measured with an objective lens of 20x magnification and the measurement of the entire eroded surface was obtained by stitching together multiple pictures into a large panorama. The measurement field area of the 20x objective is 0.81 mm by 0.81 mm and the best vertical resolution is 50 nm. The pits identified in the sample surface were distributed in size and in location. The profilometer data consisted of  $X$ - $Y$  coordinates and a depth value associated to each point. The grid resolution was 3.5226  $\mu\text{m}$  by 3.5226  $\mu\text{m}$ , leading to a minimum pit size of about 200  $\mu\text{m}^2$ , which corresponds to about a 17- $\mu\text{m}$  equivalent pit diameter.

To post-process the images, the measured sample surface was divided into sections with a maximum area of 1  $\text{mm}^2$ . This size

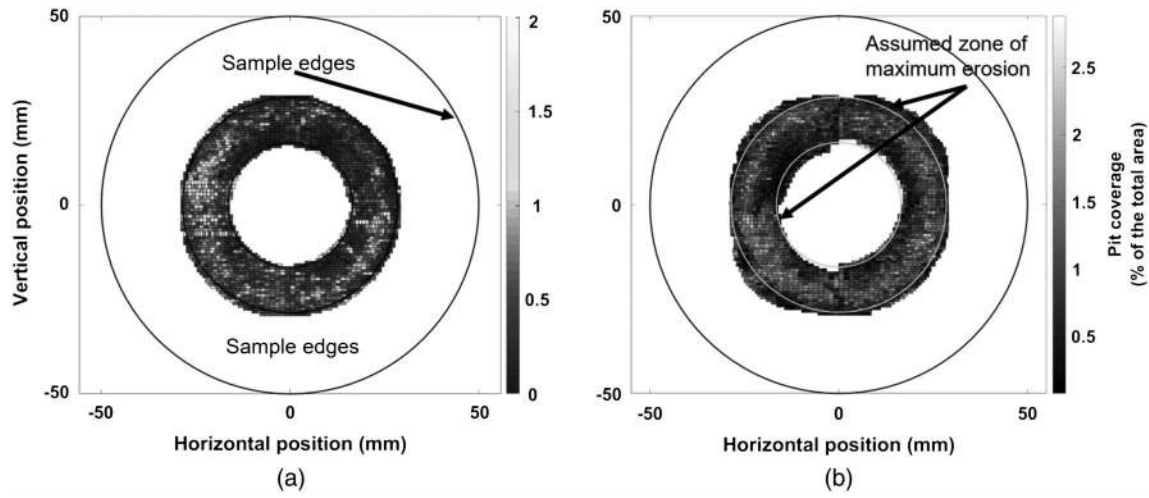


**Fig. 3.** Sample topographic sections analyzed by the optical profilometer for (a) the 2 MPa upstream pressure (6 min exposure); and (b) the 4 MPa upstream pressure (2 min exposure).

was found suitable, as detecting pits from the whole surface in one analysis would have been computationally demanding. Additionally, the measured surface was not completely flat. The overall surface level varied up to  $20 \mu\text{m}$  from edge to edge of the sample. In a  $1 \text{ mm}^2$  area, this variation was almost negligible and the surface plane could easily be corrected numerically. Since the center and outer zones are not exposed to cavitation, they were not measured. The surface area was then calculated for each detected pit. The pit coverage was defined as the sum of pit surface areas in a section, divided by section area. The pit coverage estimated from the separately analyzed sections is presented in Figs. 3(a and b), for both the 2 and 4 MPa upstream pressures.

The maximum pit coverage is substantially larger for the 4 MPa upstream pressure, as shown in Fig. 3(b). The respective exposure times were selected to lead to about the same coverage. It is however possible to compare the pitting procedures through pitting rate rather than the total amount of pits. A maximum coverage area was observed in both the samples in a ring-shaped region that corresponds to the cavity closure region, as expected. In long duration tests performed in the tunnel, there is a well-defined radius of maximum erosion rate, which should correspond to the maximum coverage area in the short duration tests. However, this is not apparent in these short duration tests, as observed from the figure. The coverage pattern is not fully axisymmetric, and this is probably a result of the random nature of the cavitation bubble and cloud collapses. Fig. 4 presents some pits detected from the profilometer data. The long scratches remaining in the surface, such as those visible in Fig. 4, were excluded from the pit analysis as explained subsequently.

The pits were first detected by setting a threshold level, and then they were characterized according to their size. The scratches originally detected as pits were elongated, so it was possible to differentiate them from pits resulting from cavitation impacts, using the shape circularity parameter  $C$  defined as:

$$C = \frac{4\pi A}{P^2} \quad (2)$$

where  $A$  = pit area and  $P$  = pit perimeter. A perfect circle has a circularity of 1 and any other shape has a circularity of less than 1. The smaller the circularity is, the more it deviates from a circle. A suitable circularity minimum of  $C = 0.75$  was selected by comparing the visualized surface, before and after excluding shapes with

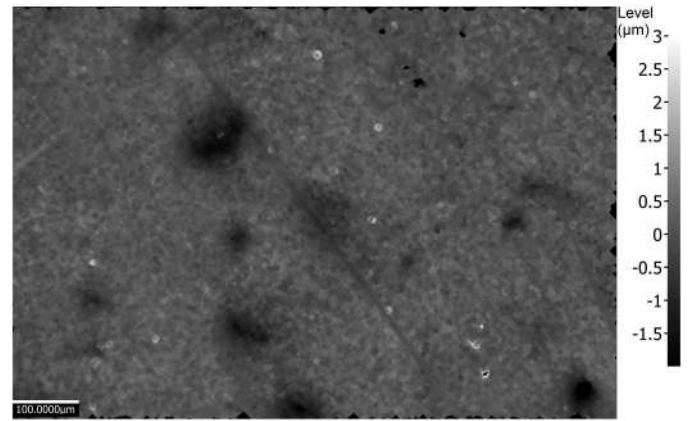


**Fig. 4.** Pit detection from the surface data in the original profilometer image.

different circularity conditions. The pits all had a more or less circular shape ( $C > 0.9$ ) whereas the scratches were noticeably elongated in shape ( $C < 0.5$ ), so it was easy to remove the latter using the threshold value.

### Measurement Uncertainty in Pit Detection

As it was impractical to include the analysis of the measurement uncertainty in the presented figures as error bars, it is discussed separately here. Assuming that the profilometer works reliably and that the algorithm detects all the pits as it should, the main uncertainty concerns the measurement of the pit diameter. The profilometer manufacturer reports a 50-nm vertical resolution, so it was assumed that such a resolution for the depth would not affect the pit detection and the diameter estimations.

Let us now focus on the error induced by the  $X$ - $Y$  measurements. As previously stated, the pixel size was  $3.5226 \mu\text{m}$ . The minimum measurable equivalent pit diameter was about  $17 \mu\text{m}$ , corresponding to five pixels. Thus, the maximum error corresponds to a case where the pit borders are either overestimated or underestimated by the pixel width. In this example, the 5-pixel diameter pit would be measured as a 3- or 7-pixel diameter pit, with erroneous pixels in both sides of the circular pit.

This rough estimate gives the upper limit of the error for the smallest measurable pits ( $\pm 7 \mu\text{m}$ ), which corresponds to twice the pixel size. The absolute error is approximately the same in the higher diameter range, as the increase or decrease of surface area is always because of an addition of a single pixel. The relative error thus decreases with increasing pit size. However, the error is typically cancelled out at least partially, as it is highly improbable for a pit to have a pixel added or removed to every point in the pit border area. More likely, some parts of the border are overestimated while some parts are underestimated, in a random pattern. Therefore, the  $7\text{-}\mu\text{m}$  error is a highly exaggerated value.

### Acoustic Emission Setup

The acoustic emission sensors were placed behind the samples, without any contact with the water flowing in the test channel. The sensors were fitted to the sample with the help of waveguides, which are steel rods with M8 screw threads in their ends. The waveguides were fixed to the material samples with the screw threads. The AE sensor is a cylinder of 20-mm diameter and 20-mm thickness. It was attached to the other end using a spring load. The waveguide length was 110.9 mm and its diameter was 12.0 mm except in the end with the screw thread. As visualized in Fig. 1(b), the contact between the waveguide and the sample was enhanced by a  $90^\circ$  countersink. To increase the elastic wave propagation through the interface, the contact surfaces were greased between the waveguide, the sensor, and the sample. Shiotani et al. (2016) explain the waveguides and the coupling medium requirements in detail.

The acquisition system was the PAC PCI-2, fitted with two sensors, the PAC R15 and the PAC D9203b, and with PAC 2/4/6 preamplifiers. Only the R15 was found to produce useful measures for the needs of this study. It has a resonance frequency of 160 kHz, as pointed out in Fig. 5 which shows the frequency response chart of the sensor. The main advantage of the R15 sensor is its sensitivity to short duration impacts, which makes it possible to distinguish individual cavitation impacts. This was observed from the waveforms, as the R15 had distinct peaks and only signal noise between impacts, compared to the D9203b that had more constant signal levels. The sampling frequency was 5 MHz, and the voltage resolution was 18 bits, which corresponds to  $76 \mu\text{V}$  for the 20 V amplitude. The signals were acquired as continuous waveforms throughout the

2- and 6-min tests. The 2/4/6 preamplifier had a 100–400 kHz band-pass analog filter. The signal was also filtered digitally in the acquisition card with the same band-pass.

## Results and Discussion

### Pit Size Distributions

To characterize the pits resulting from cavitation, the following size parameters were calculated for each pit: (1) surface area, (2) volume, (3) depth, and (4) equivalent diameter. The equivalent diameter is the diameter of an equivalent circle:

$$D = \sqrt{\frac{4A}{\pi}} \quad (3)$$

where  $D$  = pit diameter and  $A$  = pit surface area. Cumulative pit size distributions were found to be suitable for comparison between pit sizes and acoustic emission amplitude peak values. Figs. 6(a–d) presents the cumulative size distributions for all size parameters and for both operation points. The scale is linear—logarithmic.

The cumulative distribution of the pit diameter plotted in Fig. 6(a) was calculated from the pit surface distribution, using Eqs. (3) and (4). This means that the pit diameter distribution is merely proportional to the square root of the pit surface distribution. The pit diameter distribution provided the best fit in exponential distribution, i.e., it had a substantial linear part in the linear—logarithmic scale. For this reason, it was chosen as the parameter of comparison to the AE data. An exponential curve was fitted to the pit diameter distribution, marked with the dashed line in Fig. 6(a). This curve is given by the following equation:

$$\dot{N}_{\text{pit}} = \dot{N}_{0,\text{pit}} e^{-\frac{D}{D_0}} \quad (4)$$

where  $\dot{N}_{\text{pit}}$  = cumulative pitting rate,  $D$  = pit diameter, and  $D_0$  = a reference pit diameter that controls the slope of the pit distribution.  $\dot{N}_{0,\text{pit}}$  is the reference pitting rate, equal to the total pitting rate estimated by extrapolating the exponential distribution to  $D = 0$ . Let us recall here that the profilometer resolution limits the identification to pits having a diameter larger than  $17 \mu\text{m}$ . For an exponential distribution supposed to be valid for all diameters, it can easily be shown

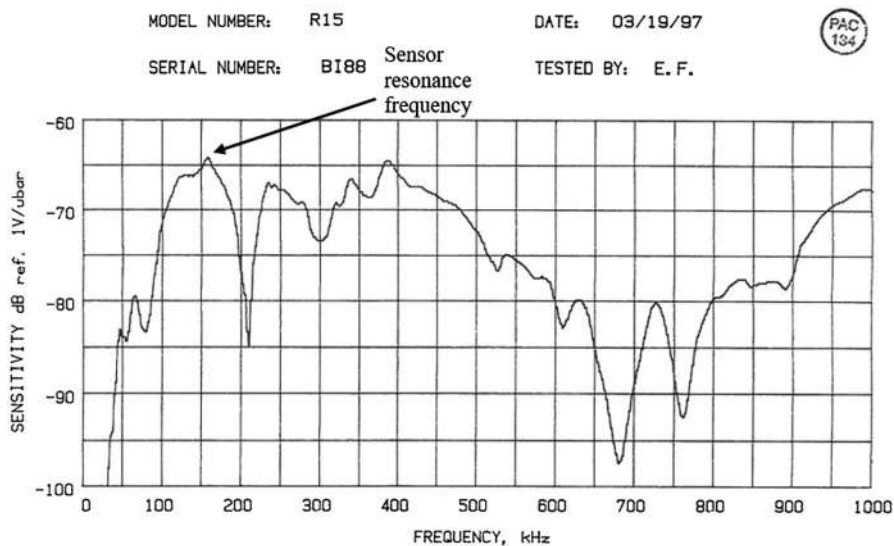


Fig. 5. PAC R15 sensor frequency response chart.

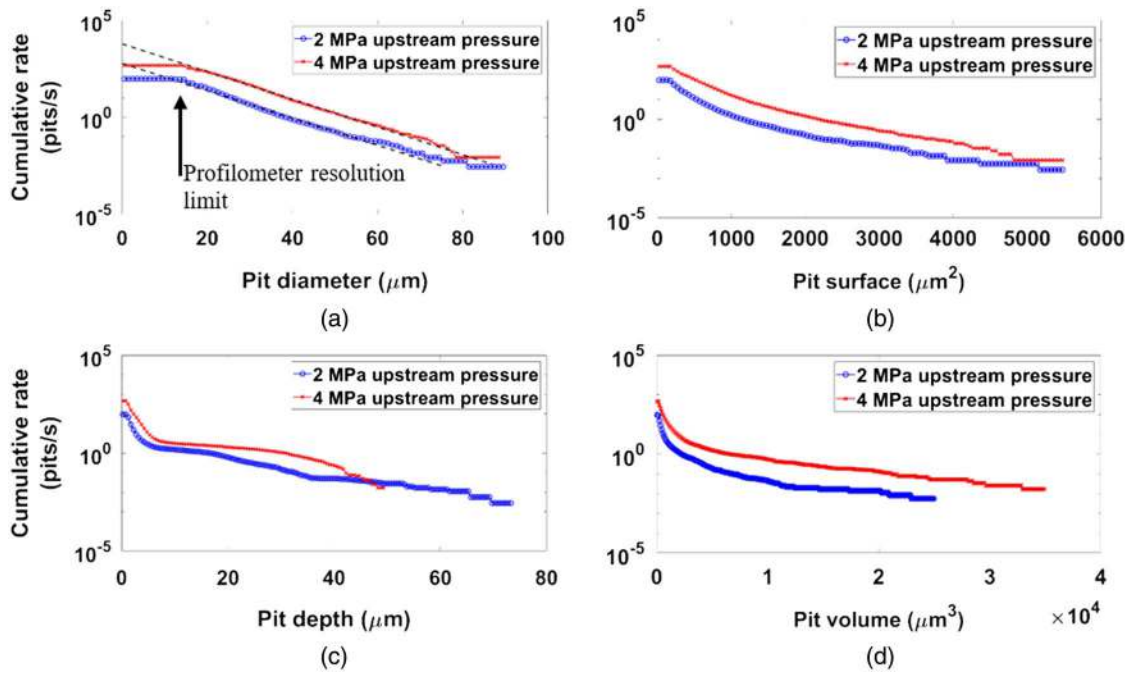


Fig. 6. Pit size cumulative distributions for both the 2 and 4 MPa upstream pressures.

that parameter  $D_0$  is the mean value of pit diameter over the whole distribution.

#### Acoustic Emission Amplitude Peak Value Distribution

To detect the events leading to the formation of the pits measured in “Pit Size Distribution,” an analysis was performed to the temporal AE signals recorded during the tests. As shown in Fig. 7, the raw AE signal consists of time on the  $X$ -axis versus voltage on the  $Y$ -axis. The signal is symmetric in the  $Y$ -direction, when the sensor is working correctly. A typical example of an AE signal recorded during an erosion test is given in Fig. 7. In Fig. 7, one can count about 40 events for the presented 11 ms window. It corresponds to a rate of about 3,600 events/s. For the full test duration, the rate of events is from 1,200 to 1,400 events/s. This means that the event

rate fluctuates significantly and a long enough time window should be considered to ensure statistical convergence of the results.

It was assumed that each burst in the AE signal corresponds to a single cavitation event. As the duration of the cavitation events is sufficiently short, the induced burst signals dissipate fast enough not to overlap with each other significantly. The higher frequency peaks within the bursts were considered as dissipating sensor resonance, as their frequency was close to the sensor resonance frequency of 160 kHz. For example, in the magnification shown in Fig. 7, the average frequency is about 150 kHz, ranging between 128 and 167 kHz. The assumption that the detected AE events correspond to damaging impacts was based on the observations by van Rijsbergen et al. (2012), who found in a hydrofoil that AE sensors attached to its shaft detect only the events occurring close enough to the hydrofoil. To detect each individual event, an envelope function

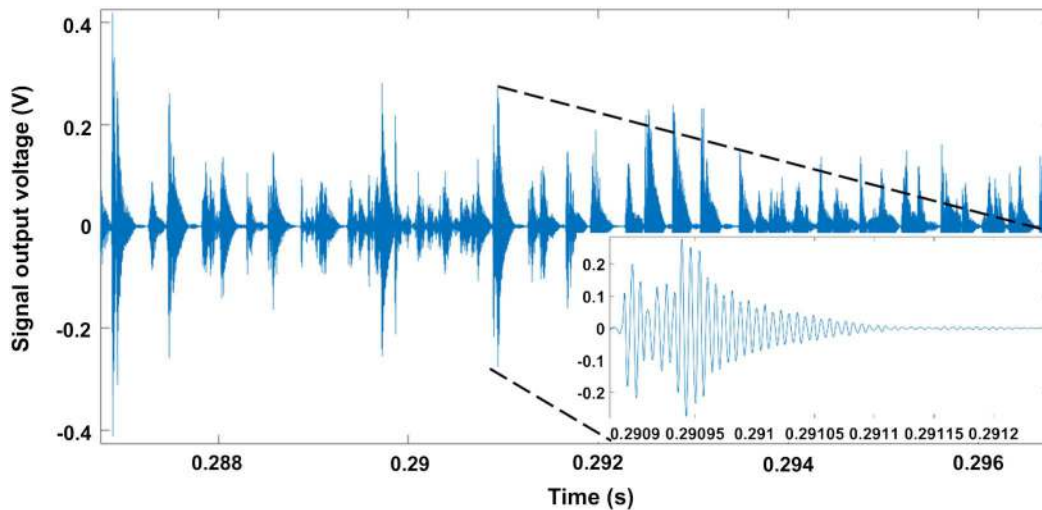
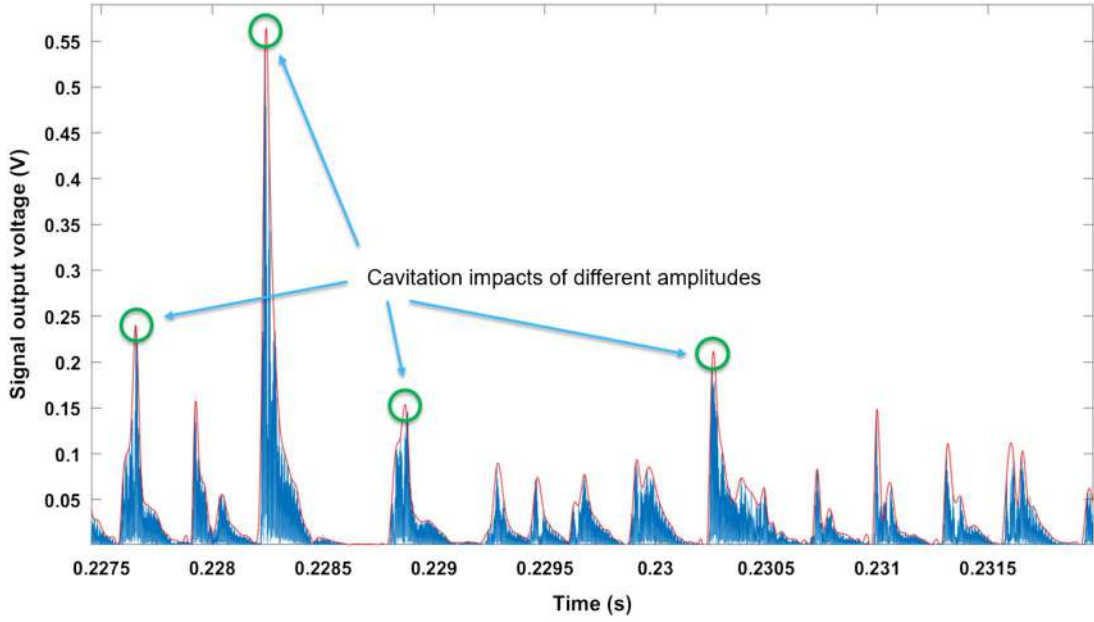


Fig. 7. R15 sensor acoustic emission signal in a cavitation test at 4 MPa upstream pressure and a zoom into one of the peaks.



**Fig. 8.** Envelope fit in the absolute value of the acoustic emission signal. The envelope function follows the acoustic emission signal main peaks, and thus ignores the higher frequency resonance effects of the sensor.

was fitted to the absolute values of all the waveforms as shown in Fig. 8. The envelope function was then used to determine the peak values of the signal amplitude.

Using this procedure, the peak values were calculated for both the 2 MPa and the 4 MPa cavitation test, for the full duration of the tests, and the amount of peaks was divided by test duration to calculate the peak rate. The cumulative distribution of the amplitude peak rate, similar to that of the pit sizes in Fig. 6, is presented in Fig. 9(c). For comparison, similar plots based on measurements by Franc et al. (2011) and by Hujer et al. (2015) are also presented in Figs. 9(a and b) respectively. Franc et al. (2011) and Hujer et al. (2015) calculated the impact loads by dropping steel balls on their sensors from different heights, thus obtaining calibration curves for the relation between impact load and peak voltage. This kind of absolute calibration of the AE sensor is not as straightforward as for pressure sensors. As the AE measurement is indirect, the signal amplitude and type depends on the location and installation of the sensor. In the installation of this study, the sensor captures events from the full sample surface, thus the response is not equal for identical impacts on different locations. Thus, the AE voltages were not transformed into any physical parameter, and only relative amplitudes were compared. This is typical in AE applications in general (Broch 1984).

The cumulative distribution for amplitude peak values shown in Fig. 9(c) has a linear part in the semi-log scale diagram, similar to the pit diameter distribution plotted in Fig. 6(a). The 4 MPa curve follows the exponential law for the whole range of data, but the 2 MPa curve tends towards the 4 MPa one for the smaller voltage values. It was assumed that this is because of the noise level arising from machine vibration and possibly from AE induced by the flow. For this reason, the linear curve was fitted only to the linear part of the distribution curve. The noise level was assumed not to vary significantly between operation points; therefore, the lowest amplitude part of the distribution should be the same for both the 2 and the 4 MPa cases. In a similar way to pit distributions, AE peak distributions were approximated by the following exponential law:

$$\dot{N}_{\text{peak}} = \dot{N}_{0,\text{peak}} e^{-\frac{U}{U_0}} \quad (5)$$

where  $\dot{N}_{\text{peak}}$  = cumulative peak rate,  $U$  = peak voltage value, and  $U_0$  = a reference peak amplitude directly related to the slope of the peak voltage value distribution.  $\dot{N}_{0,\text{peak}}$  is the total number of AE events corresponding to 0 V. The parameter  $U_0$  can be interpreted as the mean amplitude of the peaks, if the exponential distribution law is assumed to remain valid over the whole voltage range.

### Pitting Estimation from Acoustic Emission

It was assumed that the exponential curve, or the linear fit in the semi-log plot, is valid also for the small-scale events, i.e., down to  $D = 0$  for pit distributions and down to  $U = 0$  for AE peak amplitude distributions. When this assumption is valid, the  $Y$ -axis intersection of the distributions both for the pit diameter and for the AE peak rate represents the total amount of events. The results of Franc et al. (2011) and Hujer et al. (2015) also support the idea of a continuity of the exponential behavior. Fig. 10 presents a direct comparison between the cumulative pitting rate  $\dot{N}_{\text{pit}}$  and the cumulative AE peak rate  $\dot{N}_{\text{peak}}$  when plotted as a function of  $D/D_0$  and  $U/U_0$  respectively.

One can see that the total number of AE amplitude peaks is slightly larger than the total number of pits on the materials. This can be attributed to the signal noise that tends to create large amounts of small amplitude values that shift the cumulative curve to higher levels. The envelope function did not have a threshold level, so when there were no cavitation events, the signal noise was detected as small peaks. In order to improve the comparison between pitting and AE measurements, a parameter called the cut-off voltage ( $U_{\text{cutoff}}$ ) was introduced. It corresponds to the voltage value in the cumulative peak distribution for which the AE peak rate is equal to the total pitting rate extrapolated to  $D = 0$ . The cut-off voltage can be calculated from the following equation:

$$\frac{\dot{N}_{0,\text{pit}}}{\dot{N}_{0,\text{peak}}} = e^{-\frac{U_{\text{cutoff}}}{U_0}} \quad (6)$$

The cut-off voltage is visualized in Fig. 11. Effectively, the AE amplitude peak values smaller than the cut-off voltage are

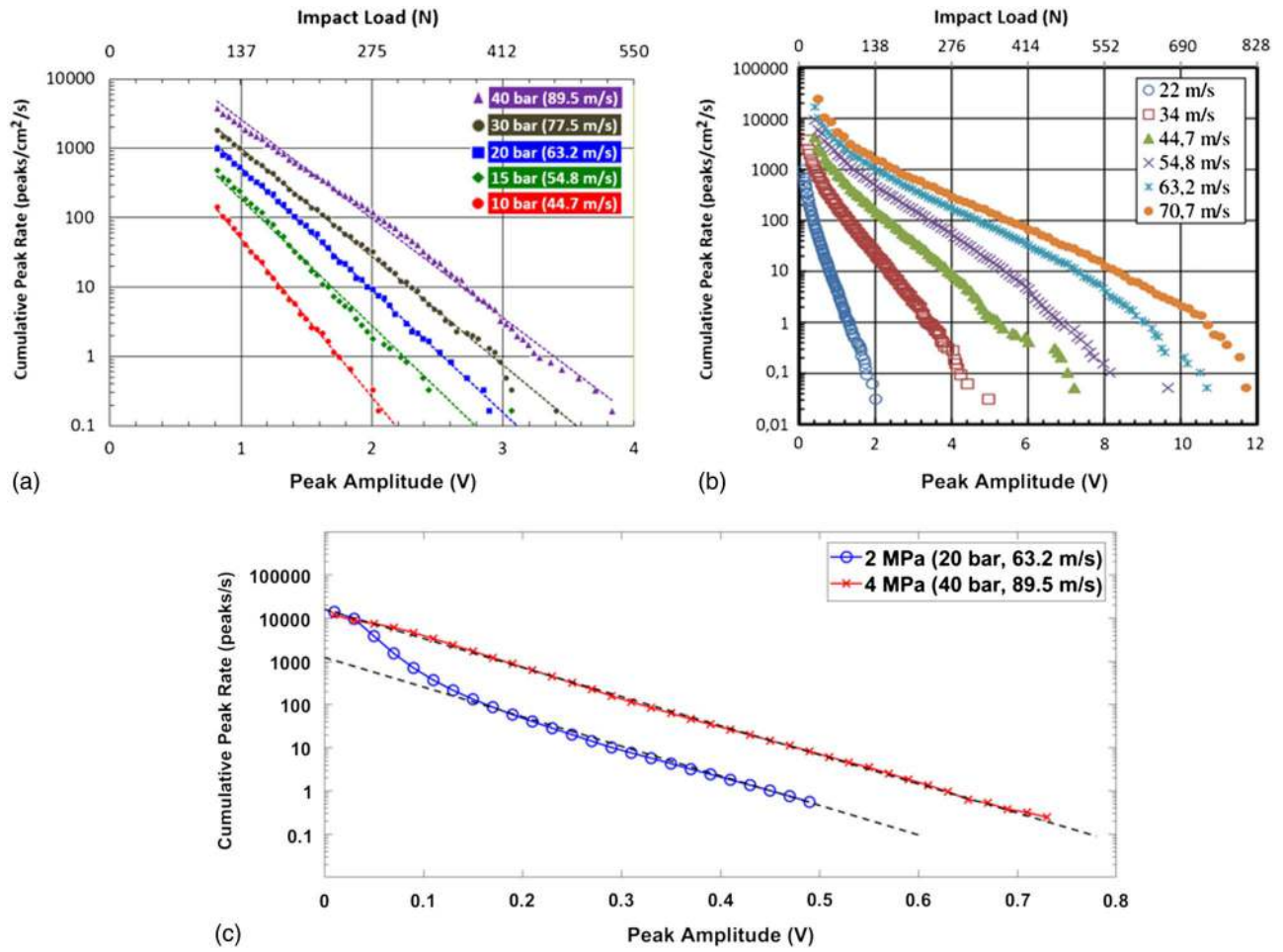


**Fig. 9.** (a) Pressure sensor cumulative peak rates (data from Franc et al. 2011); (b) PVDF sensor cumulative peak rates (data from Hujer et al. 2015); and (c) AE sensor cumulative peak rates in linear—logarithmic scale.

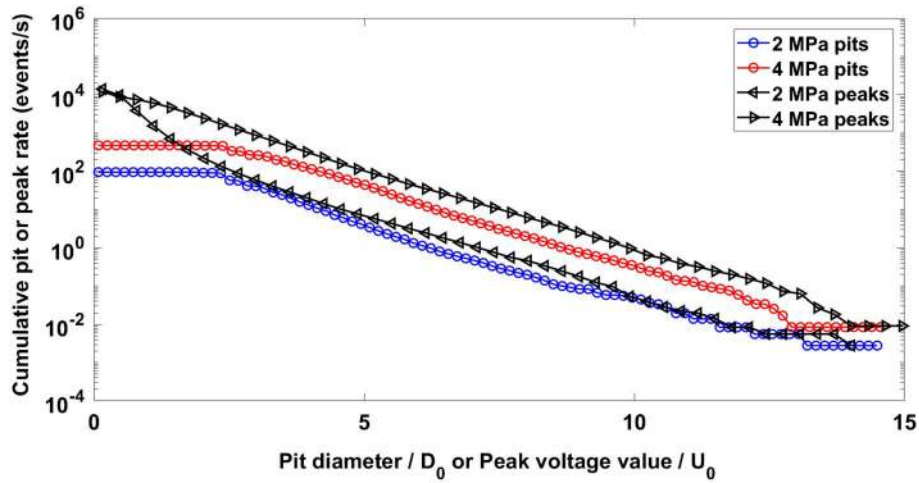


**Fig. 10.** Pit diameters and amplitude peak values normalized by the reference values, and plotted in the same graph. One notices slight overshooting of the peak amplitudes, compared to the pit diameters.

excluded from further calculations. When substituting Eq. (6) into Eq. (5), the AE peak distribution law takes the following form:

$$\dot{N}_{\text{peak}} = \dot{N}_{0,\text{pit}} e^{-\frac{U-U_{\text{cutoff}}}{U_0}} \quad (7)$$

This equation shows that the two exponential laws for the pitting rate [Eq. (4)] and for the AE peak rate [Eq. (5)] overlap when they are plotted as a function of  $D/D_0$  or  $(U-U_{\text{cutoff}})/U_0$ , respectively. As a result, a linear relation was found between amplitude peak value and pit diameter

$$\frac{D}{D_0} = \frac{U - U_{\text{cutoff}}}{U_0} \quad (8)$$

This equation allows transposing AE measurements into pit measurements. The reference values and the cut-off voltages for both the 2 and 4 MPa test cases are presented in Table 2. The total peak rates, i.e., the  $Y$ -axis intersections in Fig. 9(c), are also listed in the table.

If the distributions are normalized so that the pit diameter is divided by the reference pit diameter, while the cut-off voltage is first subtracted from amplitude peak value and then divided by the reference amplitude peak value, the distributions for both the 2 MPa and the 4 MPa operation points almost perfectly overlap, as shown in Fig. 12.

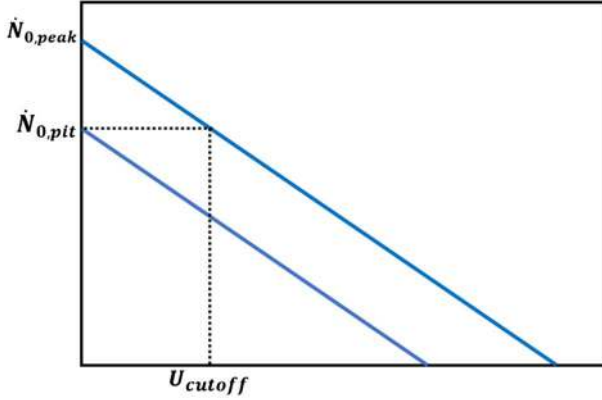


Fig. 11. Definition of the cut-off voltage.

Table 2. Pitting and AE reference values and cut-off voltages

Variable	2 MPa	4 MPa	Average
$U_{\text{cutoff}}$ (V)	0.045	0.062	0.054
$U_0$ (V)	0.064	0.065	0.064
$D_0$ ( $\mu\text{m}$ )	6.17	6.08	6.13
$U_0/D_0$ (V/ $\mu\text{m}$ )	97.28	94.22	95.75
$\dot{N}_{0,\text{pit}}$ (1/s)	598	6,070	—
$\dot{N}_{0,\text{peak}}$ (1/s)	1,232	15,958	—

The cut-off voltage  $U_{\text{cutoff}}$  is slightly changing with flow aggressiveness since it is 0.045 V at 2 MPa and 0.062 V at 4 MPa. However, compared to the whole range of the AE peak amplitudes, which is approximately 1 V, it may be acceptable to assume that it is almost constant. It can then be conjectured that this threshold is mostly material-dependent and would characterize the limit value of an AE peak that would leave a permanent pit on the material surface. A higher cut-off voltage would likely correspond to a more resistant material. Pitting tests with different materials would be necessary to confirm this trend. The reference parameters  $U_0$  and  $D_0$  are nearly constant for both the 2 and 4 MPa upstream pressures, as presented in Table 2. This means that by using the relation in Eq. (8), a pit diameter could be defined for each cavitation event, using the AE amplitude peak value. However, since the temporal location of each pit is impossible to detect during the cavitation tests, it was not found possible to relate a single peak voltage value to a single pit diameter. In other words, the presented results are statistically valid, but not necessarily for each individual bubble collapse.

The proposed method is nevertheless promising in monitoring cavitation in hydraulic machines, if developed further. Practically, several steps need to be taken. First, the pitting should be measured for a given operation point and in the area experiencing cavitation, while recording the AE signal. The transfer path from the eroding area to the sensor should be solid, and short enough to avoid significant external disturbances. The exact maximum distance is probably highly case-dependent. Second, the reference parameters  $U_0$  and  $D_0$  should be defined for the measured operation point. If it is assumed that these reference parameters remain constant in the hydraulic machine as it was in the laboratory testing, the pit diameter distribution could be then estimated for any operation point, as long as there is cavitation. Validating the extension to hydraulic machines is out of the scope of the current study.

## Conclusions

In this study, mirror-polished cylindrical stainless steel samples were subjected to cavitation erosion in a high-speed cavitation tunnel. The exposure to cavitation erosion was 2 min, when the tunnel upstream pressure was 4 MPa, and 6 min when it was 2 MPa. These relatively short exposure times are within the incubation period of cavitation erosion and they ensure that damage is limited to isolated

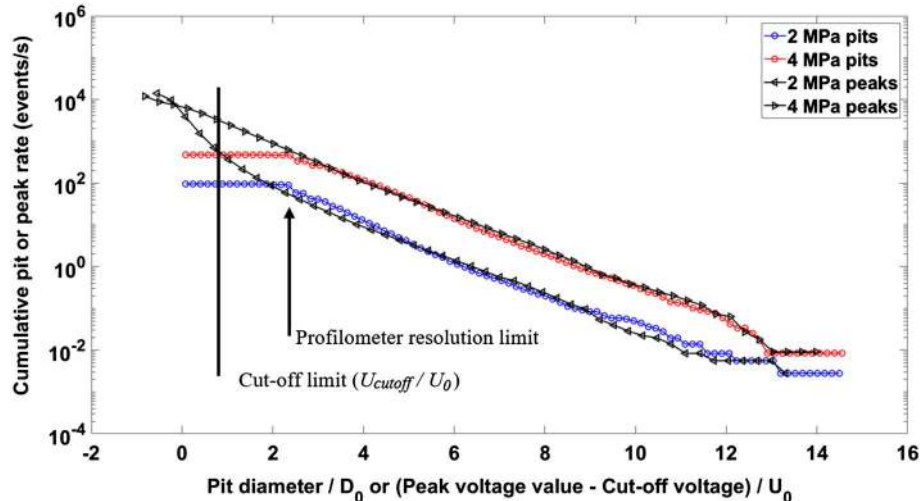


Fig. 12. Pitting and AE normalized cumulative distributions.

pits resulting from plastic deformation caused by cavitation bubble or cloud collapses. These pits were detected and measured in three dimensions using an optical profilometer. In parallel, acoustic emission was measured using a 160-kHz resonance frequency sensor with a 5-MHz sampling frequency. The complete waveforms were analyzed by peak counting from an envelope-filtered signal.

A method was presented on how to estimate cavitation pitting from the AE signal, regardless of the cavitation intensity. By introducing parameters such as the cut-off voltage, reference pit diameter and reference amplitude peak value, it was possible to establish a relationship between the cumulative distributions of amplitude peak values and pit diameters. Since the pit diameter correlates with the cavitation bubble size (Roy et al. 2015b), it is a parameter that describes, at least partially, the cavitation bubble distribution in the flow. It could be envisioned that cavitation intensity would be defined from the resulting pit diameters, but this is out of the scope of the current study. The obtained cumulative distributions for the AE signal for the two flow conditions were similar to those published by Franc et al. (2011) for pressure sensors and to those by Hujer et al. (2015) for PVDF sensors. This indicates that AE captures the correct events.

This study is limited to the incubation period of cavitation erosion. Moreover, the tests were conducted on ideal and polished samples with no initial strain, and the test duration was short. In practice, the incubation period characteristics are strongly linked to the long-term erosion rate (Franc 2009; Choi et al. 2012; Soyama and Futakawa 2004; Zhou and Hammitt 1983).

The investigated domain was limited between 2 and 4 MPa upstream pressures, so it may not be concluded that the results could be extrapolated to any situation. The cavitation in the tunnel best corresponds to that in hydrofoils; therefore, it is likely that the same relationship exists for hydrofoil tests. A common feature of the tunnel and of hydrofoils is that they may be operated in conditions leading to cloud cavitation. For extrapolation of this work to other systems, it would be preferred to seek for applications with such a cavitation type.

## Data Availability Statement

Some or all data, models, or code generated or used during the study are proprietary or confidential in nature and may only be provided with restrictions (e.g., anonymized data). All data, including the acoustic emission signal and the profilometer data are the property of the Tampere University NEM-project. The corresponding author may ask, on request, a permission from the proprietor to provide the data.

## Acknowledgments

The authors would like to thank Business Finland, Fortum Power and Heat Oy, Sandvik Mining and Construction Oy, Valtra Oy, and Teollisuuden Voima Oyj and Fortum Foundation for funding the research and for providing technical support.

## Notation

The following symbols are used in this paper:

- $A$  = pit area ( $\pi m^2$ );
- $C$  = pit circularity (-);
- $D$  = pit diameter ( $\pi m$ );
- $D_0$  = pit reference diameter ( $\pi m$ );

- $\dot{N}_{\text{peak}}$  = peak rate (1/s);
- $\dot{N}_{\text{pit}}$  = pitting rate (1/s);
- $\dot{N}_{0,\text{peak}}$  = reference peak rate (1/s);
- $\dot{N}_{0,\text{pit}}$  = reference pitting rate (1/s);
- $P$  = pit perimeter ( $\pi m$ );
- $P_d$  = downstream pressure (Pa);
- $P_u$  = upstream pressure (Pa);
- $P_v$  = vapor pressure (Pa);
- $U$  = amplitude peak value (V);
- $U_{\text{cutoff}}$  = cut-off voltage (V);
- $U_0$  = reference amplitude peak value (V); and
- $\sigma$  = cavitation number (-).

## References

- Arndt, R. E., P. Saurav, and C. R. Ellis. 1997. "Application of piezoelectric film in cavitation research." *J. Hydraul. Eng.* 123 (6): 539–548. [https://doi.org/10.1061/\(ASCE\)0733-9429\(1997\)123:6\(539\)](https://doi.org/10.1061/(ASCE)0733-9429(1997)123:6(539)).
- Arndt, R. E., R. L. Voigt, J. P. Sinclair, R. Peter, and F. Antonio. 1989. "Cavitation erosion in hydroturbines." *J. Hydraul. Eng.* 115 (10): 1297–1315. [https://doi.org/10.1061/\(ASCE\)0733-9429\(1989\)115:10\(1297\)](https://doi.org/10.1061/(ASCE)0733-9429(1989)115:10(1297)).
- Boorsma, A., and P. Fitzsimmons. 2009. "Quantification of cavitation impacts with acoustic emissions techniques." In *Proc., 7th Int. Symp. on Cavitation*, 1–6. Red Hook, NY: Curran Associates.
- Boorsma, A., and S. Whitworth. 2011. "Understanding the details of cavitation." In *Proc., 2nd Int. Symp. on Marine Propulsors*, 1–9. Hamburg, Germany: Institute for Fluid Dynamics and Ship Theory, Hamburg Univ. of Technology.
- Broch, T. J. 1984. "Acoustic emission." In *Mechanical vibration and shock measurement*, 214–219. 2nd ed. Denmark: Bruel & Kjaer.
- Carrat, J., R. Fortes-Patella, and J. Franc. 2017. "Assessment of cavitating flow aggressiveness on a hydrofoil: Experimental and numerical approaches." In *Proc., ASME 2017 Fluids Engineering Division Summer Meeting*. New York: ASME.
- Chirag, T., A. Einar, and O. G. Dahlhaug. 2018. "Experimental investigation of a Francis turbine during exigent ramping and transition into total load rejection." *J. Hydraul. Eng.* 144 (6): 04018027. [https://doi.org/10.1061/\(ASCE\)HY.1943-7900.0001471](https://doi.org/10.1061/(ASCE)HY.1943-7900.0001471).
- Choi, J., A. Jayaprakash, and G. L. Chahine. 2012. "Scaling of cavitation erosion progression with cavitation intensity and cavitation source." *Wear* 278–279 (Mar): 53–61. <https://doi.org/10.1016/j.wear.2012.01.008>.
- Franc, J. 2009. "Incubation time and cavitation erosion rate of work-hardening materials." *J. Fluids Eng.* 131 (2): 021303. <https://doi.org/10.1115/1.3063646>.
- Franc, J., M. Riondet, A. Karimi, and G. L. Chahine. 2011. "Impact load measurements in an erosive cavitating flow." *J. Fluids Eng.* 133 (12): 121301. <https://doi.org/10.1115/1.4005342>.
- Franc, J., M. Riondet, A. Karimi, and G. L. Chahine. 2012. "Material and velocity effects on cavitation erosion pitting." *Wear* 274–275: 248–259. <https://doi.org/10.1016/j.wear.2011.09.006>.
- Gangfu, Z., and C. Hubert. 2018. "Effects of step and cavity shapes on aeration and energy dissipation performances of stepped chutes." *J. Hydraul. Eng.* 144 (9): 04018060. [https://doi.org/10.1061/\(ASCE\)HY.1943-7900.0001505](https://doi.org/10.1061/(ASCE)HY.1943-7900.0001505).
- Gavaises, M., F. Villa, P. Koukouvinis, M. Marengo, and J. Franc. 2015. "Visualisation and simulation of cavitation cloud formation and collapse in an axisymmetric geometry." *Int. J. Multiphase Flow* 68 (Jan): 14–26. <https://doi.org/10.1016/j.ijmultiphaseflow.2014.09.008>.
- Grosse, C. 2008. *Acoustic emission testing*. Berlin: Springer.
- Holroyd, T. 2000. *Acoustic emission and ultrasonics handbook: Coxmoor's machine & system condition monitoring*. Moreton-in-Marsh, UK: Coxmoor Publishing Co.
- Hsiao, C., A. Jayaprakash, A. Kapahi, J. Choi, and G. L. Chahine. 2014. "Modelling of material pitting from cavitation bubble collapse." *J. Fluid Mech.* 755: 142–175. <https://doi.org/10.1017/jfm.2014.394>.

- Hujer, J., J. Carrat, M. Müller, and M. Riondet. 2015. "Impact load measurements with a PVDF pressure sensor in an erosive cavitating flow." *J. Phys. Conf. Ser.* 656 (012051): 1–4. <https://doi.org/10.1088/1742-6596/656/1/012051>.
- Look, A., O. Kirschner, S. Riedelbauch, and J. Necker. 2018. "Detection and level estimation of cavitation in hydraulic turbines with convolutional neural networks." In *Proc., 10th Int. Symp. on Cavitation (CAV2018)*, 1–4. New York: ASME.
- Momma, T., and A. Lichtarowicz. 1995. "A study of pressures and erosion produced by collapsing cavitation." *Wear* 186 (Part 2): 425–436. [https://doi.org/10.1016/0043-1648\(95\)07144-X](https://doi.org/10.1016/0043-1648(95)07144-X).
- Neill, G. D., R. L. Reuben, P. M. Sandford, E. R. Brown, and J. A. Steel. 1997. "Detection of incipient cavitation in pumps using acoustic emission." *Proc. Inst. Mech. Eng.* 211 (4): 267–277. <https://doi.org/10.1243/0954408971529737>.
- Ohtsu, M. 2008. "Sensor and instrument." In *Acoustic emission testing*, edited by C. Grosse and M. Ohtsu, 19–40. Berlin: Springer.
- Penghua, T., and Y. James. 2018. "Modeling and prototype testing of flows over flip-bucket aerators." *J. Hydraul. Eng.* 144 (12): 04018069. [https://doi.org/10.1061/\(ASCE\)HY.1943-7900.0001531](https://doi.org/10.1061/(ASCE)HY.1943-7900.0001531).
- Poddar, S., and N. Tandon. 2016. "Detection of journal bearing vapour cavitation using vibration and acoustic emission techniques with the aid of oil film photography." *Tribol. Int.* 103 (Nov): 95–101. <https://doi.org/10.1016/j.triboint.2016.06.039>.
- PREVERO. 2018. "The PREVERO cavitation erosion tunnel." Accessed October 25, 2018. <http://web.archive.org/web/20180327065723/http://www.legi.grenoble-inp.fr/web/spip.php?article1265&lang=fr>.
- Roy, S. C., J. Franc, and M. Fivel. 2015a. "Cavitation erosion: Using the material as a pressure sensor." *J. Appl. Phys.* 118 (16): 164905. <https://doi.org/10.1063/1.4934747>.
- Roy, S. C., J. Franc, N. Ranc, and M. Fivel. 2015b. "Determination of cavitation load spectra—Part 2: Dynamic finite element approach." *Wear* 344–345 (Dec): 120–129. <https://doi.org/10.1016/j.wear.2015.09.005>.
- Schmidt, H., O. Kirschner, and S. Riedelbauch. 2015. "Cavitation measurements on a pump-turbine model." *J. Phys. Conf. Ser.* 656 (012051): 1–4. <https://doi.org/10.1088/1742-6596/656/1/012071>.
- Schmidt, H., O. Kirschner, S. Riedelbauch, J. Necker, E. Kopf, M. Rieg, G. Arantes, M. Wessiak, and J. Mayrhuber. 2014. "Influence of the vibro-acoustic sensor position on cavitation detection in a Kaplan turbine." In Vol. 22 of *Proc., IOP Conf. Series: Earth and Environmental Science*, 1–9. Bristol, UK: IOP Publishing.
- Shiotani, T., Y. Mizutani, H. Nakamura, and S. Yuyama. 2016. "Practical AE testing, data recording and analysis." In *Practical acoustic emission testing*, 67–72. New York: Springer.
- Soyama, H., and M. Futakawa. 2004. "Estimation of incubation time of cavitation erosion for various cavitating conditions." *Tribol. Lett.* 17 (1): 27–30. <https://doi.org/10.1023/B:TRIL.0000017415.79517.8c>.
- van Rijsbergen, M., E. Foeth, P. Fitzsimmons, and A. Boorsma. 2012. "High-speed video observations and acoustic-impact measurements on a NACA 0015 Foil." In *Proc., 8th Int. Symp. on Cavitation (CAV 2012)*, 958–964. Singapore: Research Publishing Services.
- Wang, Y., and Y. Chen. 2007. "Application of piezoelectric PVDF film to the measurement of impulsive forces generated by cavitation bubble collapse near a solid boundary." *Exp. Therm Fluid Sci.* 32 (2): 403–414. <https://doi.org/10.1016/j.expthermflusci.2007.05.003>.
- Zhou, Y., and F. G. Hammit. 1983. "Cavitation erosion incubation period." *Wear* 86 (2): 299–313. [https://doi.org/10.1016/0043-1648\(83\)90168-0](https://doi.org/10.1016/0043-1648(83)90168-0).